Chemical Science

ROYAL SOCIETY OF CHEMISTRY

EDGE ARTICLE

View Article Online
View Journal | View Issue

Cite this: *Chem. Sci.*, 2025, **16**, 13070

All publication charges for this article have been paid for by the Royal Society of Chemistry

Single electron/energy transfer photocatalysis: α-/β-switchable synthesis of 3-deoxy-D-manno-oct-2-ulosonic acid *O*-glycosides†

Jing-dong Zhang, ‡ Jia-long Jie, ‡* Shu-yi Yan, Hui Zhang, Jia-meng Chen, Jiang-cheng Wu, Lu-yang Qin, Guang-jian Liu, Hong-mei Su and Guo-wen Xing *

Stereoselective glycosidation of 3-deoxy-D-manno-oct-2-ulosonic acid (Kdo) has emerged as a focal point in glycoscience, attributed to the burgeoning identification of naturally occurring α- or β-Kdo glycosides within the glycoconjugate structures of various organisms. Nonetheless, advancements in α-/β-switchable stereoselective Kdo *O*-glycosidation remain scarce due to the complicated synthesis of Kdo donors and the complex chemical environment at the anomeric carbon of Kdo. Herein, inspired by the property that the conditions of the photocatalytic reaction can be facilely controlled and mediated, we report an efficient photocatalytic Ir^{III}/Cu^{II}-catalysed Kdo *O*-glycosidation for the stereoselective synthesis of both α- and β-Kdo *O*-glycosides with the dual mediation of MeCN and $(p\text{-Tol})_2SO$. Within a facile photoreactor, the glycosidation reactions were carried out at −78 °C to generate β-Kdo *O*-glycosides in excellent yields (up to 99%) *via* the glycosyl nitrilium ion, and at −30 °C to generate α-Kdo *O*-glycosides in good yields (57–99%) *via* the oxosulfonium ion. Two crystals of α-Kdo *O*-glycosides were cultivated to assess the stereochemical configurations. Subsequently, laser flash photolysis, steady-state measurement and ESR spectral measurement were conducted to first reveal a single electron transfer (SET) together with the Dexter energy transfer (EnT) process of the photocatalytic activation by monitoring the trifluoromethyl radical, the cation radical of dibenzothiophene and the cation radical of 4,5,7,8-tetra-*O*-acetyl-Kdo *p*-toluenethioglycoside. (TD)-DFT calculations further supported this process and illustrated a S_N2-like mechanism for the attack of hydroxyl acceptors.

Received 23rd April 2025
Accepted 11th June 2025

DOI: 10.1039/d5sc02980e

rsc.li/chemical-science

Introduction

3-Deoxy-D-manno-oct-2-ulosonoic acid (Kdo) is a non-mammalian eight-carbon monosaccharide.[1,2] Kdo mostly exists as α-Kdo glycosides in nature, which are the smallest unit of Kdo_2-lipid A in the lipopolysaccharide (LPS) of Gram-negative bacteria.[3] In contrast, the β-Kdo glycosides are mainly located in bacterial capsular polysaccharides (CPSs)[4] as well as the extracellular exopolysaccharides (EPS)[5] (Fig. 1, **1**–**3**). β-Kdo disaccharide unit **4** was also found in the core region of LPS from *Proteus vulgaris* serotype O25. Moreover, in the biosynthetic pathway of natural Kdo glycosides, cytidine-5′-monophospho-Kdo **5** (CMP-Kdo), features a β-linkage of the Kdo moiety to facilitate the assembly of bacterial glycans as the principal substrate for glycosyltransferases.[6]

Since Kdo glycosides can be recognized by the human native and adaptive immune systems, the stereoselective synthesis of Kdo glycosides has attracted increasing attention in recent years.[7] However, stereoselective and efficient synthesis of Kdo glycosides remains a great challenge, due to the presence of the electron-withdrawing carboxylic group at the C1 position, which not only reduces the reaction activity but also allows the elimination reaction to occur more easily to generate the 2,3-glycal

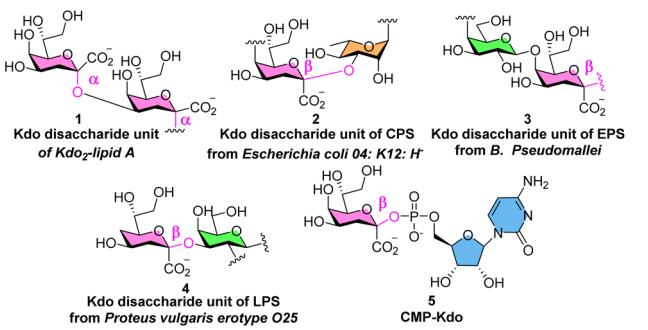

Fig. 1 Naturally occurring compounds containing the Kdo structure.

College of Chemistry, Beijing Normal University, Beijing 100875, P. R. China. E-mail: gwxing@bnu.edu.cn; jialong@bnu.edu.cn

† Electronic supplementary information (ESI) available. CCDC 2382908 and 2382909. For ESI and crystallographic data in CIF or other electronic format see DOI: https://doi.org/10.1039/d5sc02980e

‡ J.-d. Zhang and J.-l. Jie contributed equally to this work.

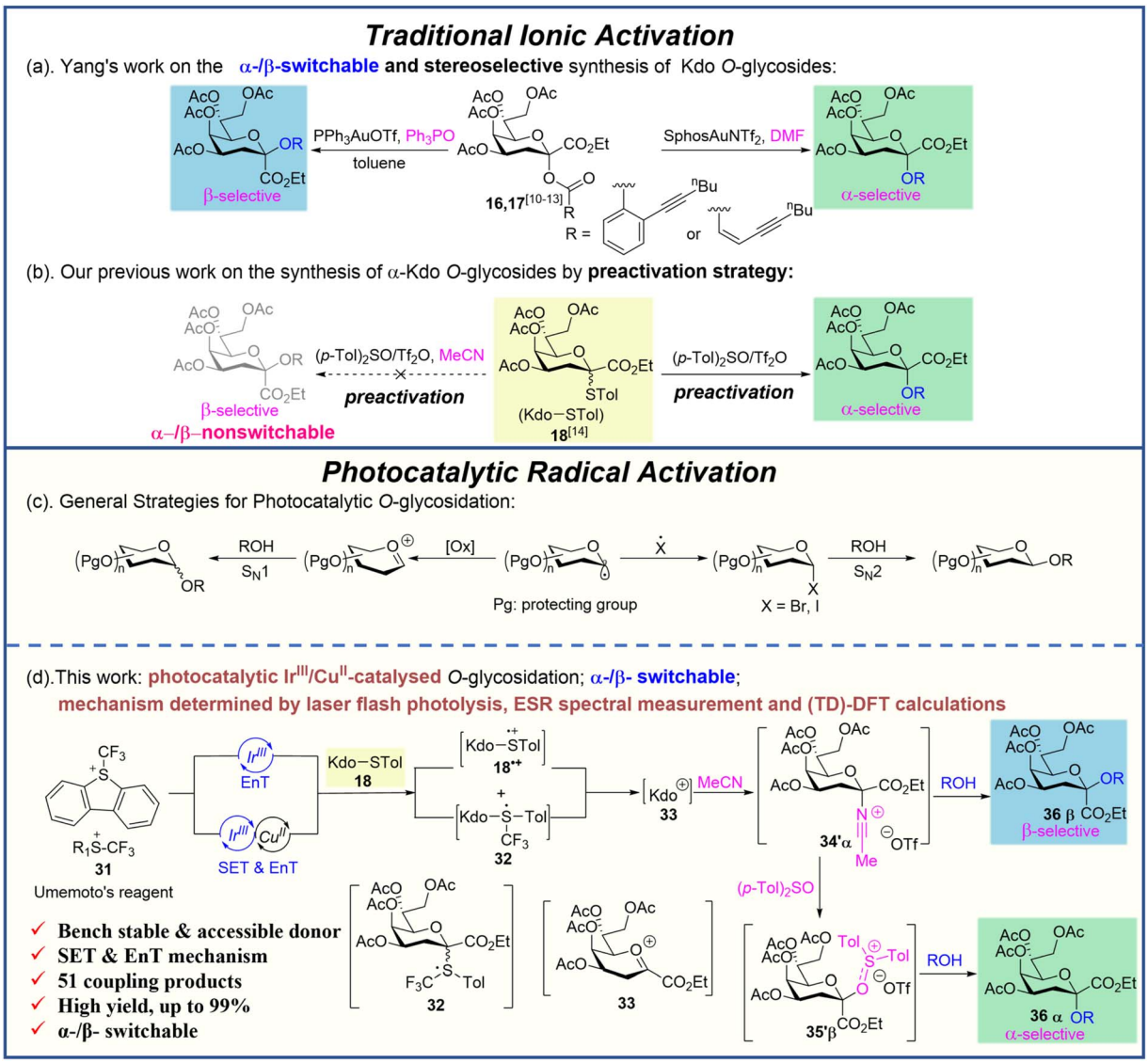

Scheme 1 Brief introduction of α-/β-stereoselective Kdo *O*-glycosidation, photocatalytic *O*-glycosidation and our photocatalytic Ir^{III}/Cu^{II}-catalysed Kdo *O*-glycosidation.

byproduct. In addition, the lack of a hydroxyl group at the C3 position makes it difficult to completely control the stereochemistry of the glycosidation reaction by using the neighboring group participation.[7,8]

In recent years, based on the ionic activation mechanism, various strategies[7,9] have been developed for the efficient synthesis of α-Kdo glycosides (Fig. S1,† **6–25**) or β-Kdo glycosides (Fig. S1,† **26–30**). Nevertheless, only the Au(I)-catalyzed Kdo *O*-glycosidation developed by Yang's group[10–13] achieved the α-/β-switchable stereoselective Kdo *O*-glycosidation by adding DMF or not (Scheme 1a). Recently, using the 4,5,7,8-tetra-*O*-acetyl-Kdo *p*-toluenethioglycoside **18** as the donor, by the (*p*-Tol)$_2$SO/Tf$_2$O preactivation strategy, our group successfully obtained α-Kdo *O*-glycosides (Scheme 1b) with the mediation of excess (*p*-Tol)$_2$SO, but failed to synthesize the β-Kdo *O*-glycosides with the mediation of acetonitrile (MeCN).[14] Therefore, a more general and efficient method for stereoselectively synthesizing both α- and β-Kdo glycosides with high yields and accessible donors still needs to be developed.

Photocatalytic reactions, due to their controllable reaction conditions and widespread applications in organic synthesis, have attracted a lot of attention from more and more scientific researchers.[15–17] However, photocatalysis is addressed relatively less in carbohydrate chemistry, especially in *O*-glycosidation.[18] To obtain *O*-glycosides during glycosidation, usually the nucleophile needs to attack the widely accepted intermediate oxacarbenium ion, while in photocatalytic glycosidation the special intermediate glycosyl radical needs to attack the double bond or combine with the transition metal catalyst to achieve *C*-glycosides or *N*-glycosides, which means that such a radical process tolerates hydroxyl groups.[18] Thus, two different methods for generating *O*-glycosides during photocatalytic glycosidation were developed in recent years (Scheme 1c). One is to oxidize the glycosyl radicals into oxacarbenium ions or directly

generate them with light induced catalytic activation.[19–24] The other is to transfer the glycosyl radicals into less active glycosides such as bromo glycosides[25] and iodine glycosides[26] to obtain the target products through the S_N2 process.

Umemoto's reagent, as the precursor of the highly electrophilic trifluoromethyl radical ($CF_3^{\bullet}$), was disclosed to activate thioglycoside donors[20,21] or selenoglycoside donors[24] for the synthesis of *O*-glycosides. However, the detailed mechanism of photocatalytic *O*-glycosidation with thioglycoside as the donor and Umemoto's reagent as the promoter remained obscure. Furthermore, to date, no photocatalytic Kdo glycosidations have been reported.

Herein, considering the increasing importance of both α- and β-Kdo glycosides[3–7,27] and the versatility of the accessible thioglycoside donors,[14,28,29] we reported a photocatalytic **Ir^{III}/Cu^{II}**-catalysed and MeCN/(p-Tol)$_2$SO dual mediated Kdo *O*-glycosidation using 4,5,7,8-tetra-*O*-acetyl-Kdo *p*-toluenethioglycoside **18** as the donor, Ir[dF(CF_3)ppy]$_2$(dtbbpy)PF_6 (**Ir^{III}**) as the photocatalyst and Umemoto's reagent as the light-driven activator for the stereoselective synthesis of both α- and β- Kdo *O*-glycosides (Scheme 1d). Moreover, detailed mechanism studies were conducted to clarify the reaction process of photocatalytic glycosidation.

Results and discussion

Glycosidation study

To determine the stereochemistry of Kdo glycoside, the selective proton decoupled ^{13}C NMR spectra were used to obtain the coupling constant between the H_{ax} at C3 and the carbon atom at the C1-position ($^3J_{C1/H3axial}$).[30] Generally, the $^3J_{C1/H3axial}$ value of α-anomer is ≤1.0 Hz, while the β-anomer's value is 5.0–6.0 Hz.[31]

According to the previous reports on Kdo glycosidation,[7] it is necessary to conduct the glycosidation reactions at low temperatures to achieve better stereoselectivities and higher yields. Consequently, we designed and constructed a facile, accessible, and cost-effective photocatalytic glycosidation apparatus for this study (Fig. 2). The apparatus comprises an inexpensive LED light strip integrated within a glass helical tube, a reaction flask, and a low-temperature thermostatic reaction bath. The glass helical tube enables the direct immersion of the LED light strip in ethanol, thereby facilitating a photocatalytic reaction within the bath at low temperatures. The external lighting apparatus allows for superior sealing of the reaction environment. Based on the low power consumption of the LED light source, the reaction can be safely maintained for prolonged periods.

Fig. 2 The photocatalytic glycosidation apparatus designed, constructed and applied in this work.

Table 1 Comparison of reaction components

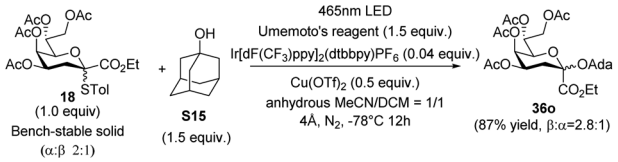

Entry	Variation from labelled conditions	Yield[a]	$\beta:\alpha^b$
1	None	87%	2.8 : 1
2	No Umemoto's reagent	$6\%^{94\%}$	1.5 : 1
3	No light	NR	ND
4	1 : 1 instead of 2 : 1 (the α/β ratio of donors)	88%	2.8 : 1
5	3.0 equiv. of PBN as the additive	NR	ND
6[c]	3.4 equiv. of (p-Tol)$_2$SO as the additive	99%	1 : 13

[a] Isolated yields and superscripts indicating the amount of donor regained. [b] Determined by ^1H NMR. [c] 1.5 equiv. of Cu(OTf)$_2$ and reacting at −30 °C with MeCN/DCM = 2/1 as the solvent. NR: not reaction. ND: not determined.

The model photocatalytic glycosidation between Kdo thioglycoside donor **18** and 1-adamantanol **S15** (Fig. S2†) was conducted under specific conditions (Table S1,† entry 1), resulting in moderate yield (70%) but poor stereoselectivity ($\alpha:\beta = 1.4:1$). Since the glycosidation reactions are complex and affected by many factors,[32] the optimization of the photocatalytic glycosidation reaction was carried out based on multiple factors respectively (Tables 1 and S1–S5†).

To verify the oxidative effect of Cu(OTf)$_2$ (**Cu^{II}**) in photocatalytic Kdo *O*-glycosidation, a series of experiments were performed as shown in Table S1.† The results showed that **Cu^{II}** could accelerate the process of the reaction as the catalyst, which improved the activation of donors (Table S1,† entry 3 and 5). Besides, when changing the amount of Cu(OTf)$_2$, the stereoselectivity of glycosidation was constant (Table S1,† entry 1–5), indicating that **Cu^{II}** could not participate in the process of nucleophilic attack of acceptors.

Since temperature is a key factor for the reaction, especially in Kdo glycosidation reactions,[14,32] the influence of temperature was investigated carefully (Table S2†). Apparently, lower temperature could benefit the stabilization of the reactive intermediate and lead to higher yield (−78 °C, 87%, $\beta:\alpha = 2.8:1$). It was worth noting that there was a transition of the stereoselectivity from α to β with the decrease in temperature (Table S2,† entry 2–5). Considering the effect of acetonitrile in the glycosidation reaction,[28] the mixed solvent system was changed to clarify the relationship between solvent and Kdo glycosidation (Table S3†). On reducing the amount of acetonitrile, both the yield and the β-stereoselectivity decreased, indicating that acetonitrile could control the stereoselectivity by reacting with the reactive intermediate oxacarbenium ion **33** to form the more stable intermediate glycosyl nitrilium ions **34′α** (Scheme 1c). Further density functional theory (DFT) calculation and analysis[33] supported such a conclusion (Scheme 5).

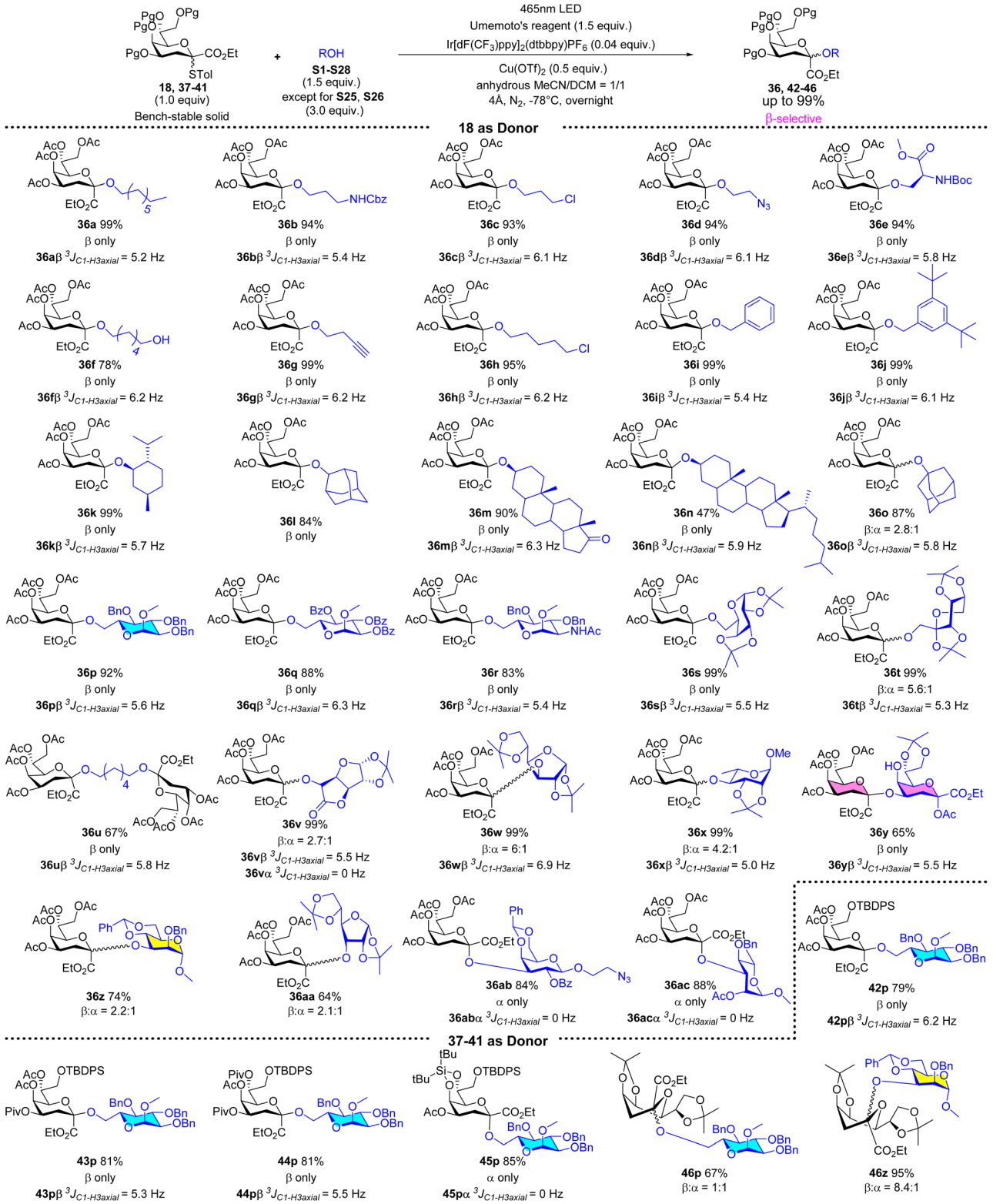

Scheme 2 β-Selective photocatalytic Kdo *O*-glycosidation of **18** with a series of acceptors and **37–41** with **S16** as the acceptor.

Based on our previous work on the $(p\text{-Tol})_2SO/Tf_2O$ pre-activation strategy of Kdo *O*-glycosidation,[14] $(p\text{-Tol})_2SO$ is an important additive that could efficiently modulate reaction yields and lead to α-stereoselectivities by forming the reported and verified oxosulfonium salts **35** (ref. 14, 34 and 35) (Scheme 1c). Thus, the effect of the amount of $(p\text{-Tol})_2SO$ on the photocatalytic Kdo *O*-glycosidation was investigated carefully, as shown in Table S4.† To our delight, $(p\text{-Tol})_2SO$ as an additive

could obviously improve both the yield and the α-stereoselectivity of the photocatalytic Kdo *O*-glycosidation (Table 1, entry 6). However, adding excess $(p\text{-Tol})_2SO$ to 4.0 equivalent led to a decrease in yield (Table S4,† entry 2–3), suggesting that the excess $(p\text{-Tol})_2SO$ could suppress the activation reaction of the donor.

Photocatalysts (PC) were also evaluated (Table S5†). It was found that PC had a weak correlation with the stereoselectivity of glycosidation but strong correlation with the yield of glycosidation, indicating that the PC could not participate in the nucleophilic attack of acceptors towards the reactive intermediate but only influenced the activation of the donor. It was important to note that the yield was highly correlated with the $E_{1/2\ PC^+/PC}$, indicating that the PC^+ species could be a vital part of the photocatalytic cycle.

Next, the preliminary studies on the mechanism of photocatalytic Kdo *O*-glycosidation were conducted as shown in Table 1. The photocatalytic Kdo *O*-glycosidation was not affected by the α/β ratio of Kdo donors (Table 1, entry 1 and 4), showing that the target products were produced through the intermediates instead of the glycosyl donors. Furthermore, the addition of *N*-*tert*-butyl-α-phenylnitrone (PBN) as the radical scavenger significantly suppresses the reaction, thereby suggesting that the reaction was initiated through the generation of radical species (Table 1, entry 2, 3 and 5).

Under the optimized reaction conditions (1.0 equiv. of **18**, 1.5 equiv. of acceptor, 1.5 equiv. of Umemoto's reagent, 0.04 equiv. of $Ir[dF(CF_3)ppy]_2(dtbbpy)PF_6$, and 0.5 equiv. of $Cu(OTf)_2$, −78 °C 12 h, in acetonitrile/dichloromethane = 1/1), a series of glycosyl acceptors shown in Fig. S2† were examined for the Kdo glycosidation reactions. As shown in Scheme 2, when primary or secondary non-carbohydrate alcohols (**S1–S14**) were used as acceptors to be coupled with **18**, the desired β-Kdo *O*-glycosides (**36aβ–36nβ**) were successfully obtained in favorable yields (78–99%) and excellent stereoselectivities. Since dihydrocholesterol **S14** had poor solubility in acetonitrile and its mixed solvent, the yield was moderate (47%) compared with epiandrosterone **S13** (90%). For tertiary alcohol 1-ada, due to its larger steric hindrance and weaker nucleophilic properties, glycosidation might proceed *via* an S_N2-like mechanism, resulting in moderate β-stereoselectivity (**36o**, $\alpha/\beta = 1:2.7$). On employing sugar alcohols as acceptors, the glycosidation reactions were more complicated. For primary sugar alcohols **S16–S20** as acceptors, Kdo glycosidation with **18** also furnished excellent β-selective *O*-glycosides (**36pβ–36tβ**) in high yields (83–99%). But for secondary sugar alcohols or their derivatives as acceptors,

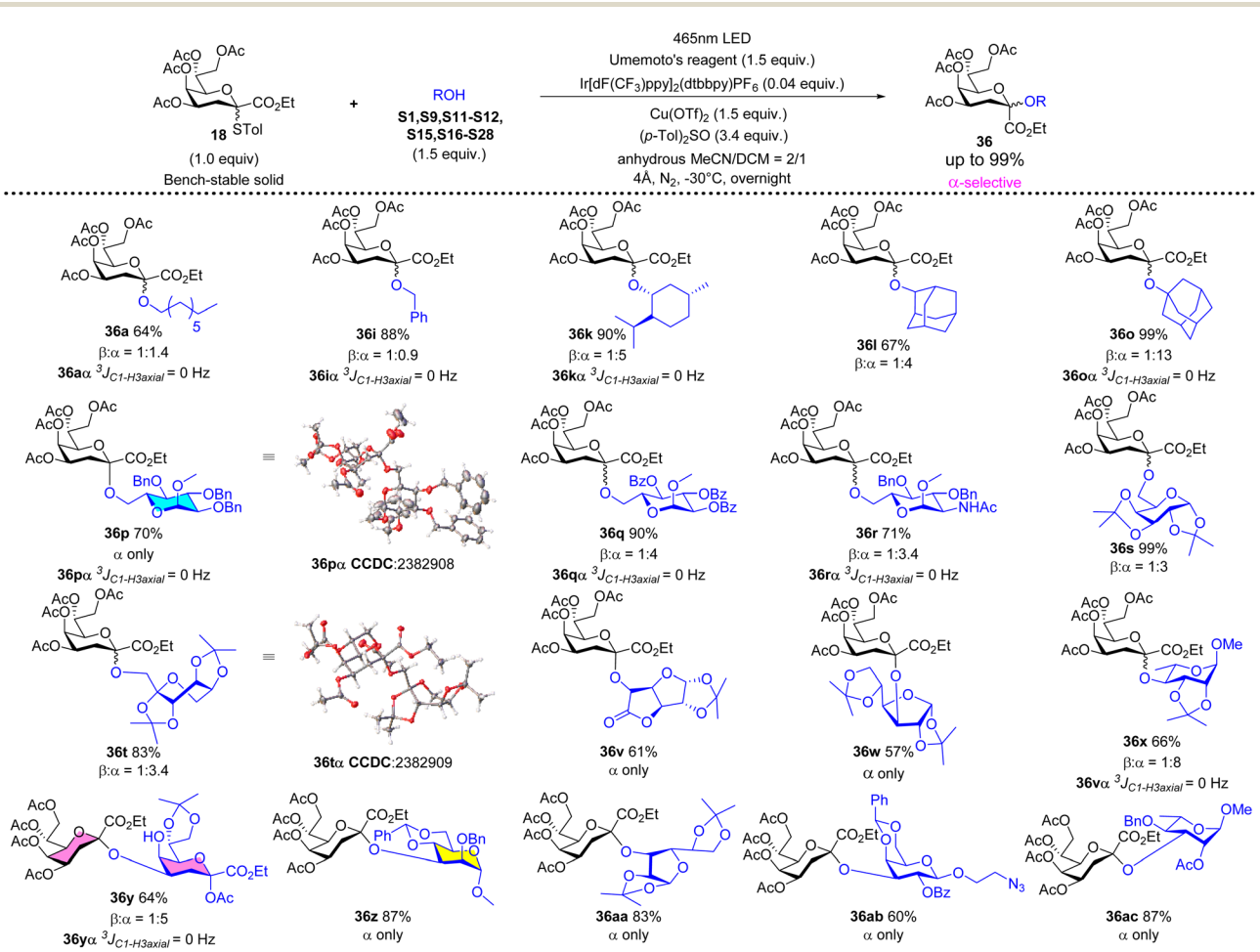

Scheme 3 α-Selective photocatalytic Kdo *O*-glycosidation of **18** with a series of acceptors.

the results showed that the stereoselectivities of glycosidation depended on the steric hindrance of acceptors (**36v–36ac**). Greater steric hindrance and less nucleophilic ability might cause the mechanism to be S_N1-like, leading to poor β-stereoselectivity (**36z** and **36aa**) or α-stereoselectivity (glycosyl *cis*-diol **S27** as the acceptor to generate **36abα** and glycosyl *cis*-diol **S28** as the acceptor to generate **36acα**, respectively). Notably, using 0.5 equivalent of 1,6-hexanediol **S6** in glycosidation, the desired pseudo β-Kdo disaccharide **36uβ** was obtained in a good yield (67%). Moreover, the β-Kdo-(2 → 4)-α-Kdo-OAc disaccharide **36yβ** was successfully obtained in good yield (65%) using this strategy, demonstrating the method's excellent tolerance for glycosyl acetates, which contrasts with traditional ionic glycosidation.

On changing the protecting group from the acetyl group to other electron-withdrawing protecting groups (Piv, **37–39**, Scheme S1†) the reactivity and stereoselectivity could be maintained to generate β-Kdo *O*-glycosides (**42pβ–44pβ**) in high yields. For Si-protected donor **40** (Scheme S1†), it could be effectively activated, although the regulatory role of acetonitrile is not significant in this case. The product was α-Kdo *O*-glycoside **45pα**, indicating that the bulky protecting group effectively restricted the reaction space on the donor's β-face.[9e] Additionally, when using armed Kdo glycosyl donor **41** (Scheme S1†) to furnish *O*-glycosides (**46p** and **46z** (ref. 28)), the role of acetonitrile was consistent with that reported in the traditional ionic activation glycosidation.

Adding $(p\text{-Tol})_2SO$ as the additive in photocatalytic Kdo *O*-glycosidation could change the stereoselectivity from β-to α-anomer. Under the optimized reaction conditions (1.0 equiv. of **18**, 1.5 equiv. of acceptor, 1.5 equiv. of Umemoto's reagent, 0.04 equiv. of $Ir[dF(CF_3)ppy]_2(dtbbpy)PF_6$, 1.5 equiv. of $Cu(OTf)_2$, and 3.4 equiv. of $(p\text{-Tol})_2SO$, −30 °C 12 h, in $MeCN/CH_2Cl_2 = 2/1$), the switchable phenomenon of stereoselectivity was explored using different types of acceptors. As shown in Scheme 3, using primary non-carbohydrate alcohols (1-octanol **S1** or benzyl alcohol **S9**) as acceptors could not achieve such goals (**36a** and **36i**, $\alpha/\beta \approx 1:1$), because of their strong nucleophilic properties and less steric hindrance which lead to the competition between the attack of primary alcohols and the attack of $(p\text{-Tol})_2SO$ towards the glycosyl nitrilium ions. Surprisingly, for other non-primary alcohols (**S11–S12**, **S15**, and **S21–28**) and primary sugar alcohols (**S16–S20**), based on their weaker nucleophilic properties and larger steric hindrance, the switchable phenomenon of stereoselectivity was successfully achieved (**36k**, **36l**, **36o**, **36p–36t**, **36v–36ac**, $\alpha/\beta > 3:1$) in good yields (57–99%). The single crystal structures of **36pα** and **36tα** were obtained to further determine the absolute stereochemical configurations. When using Kdo glycosyl acetate **S24** as the acceptor, the desired α-Kdo-(2 → 4)-α-Kdo-OAc disaccharide **36yα**, which is the Kdo disaccharide unit of Kdo_2-lipid A, could be obtained in a good yield (64%) with high α-stereoselectivity.

Besides, scale-up reactions were conducted to evaluate the pragmatic value of the present method and designed apparatus (Table 2). It was shown that such a reaction could efficiently proceed at the milligram scale level. However, at the gram scale level, limited by the size of the photoreactor, the activation of donors was 60% resulting in moderate yields (59%) while the configuration remained β-selective.

Table 2 Scale-up reaction

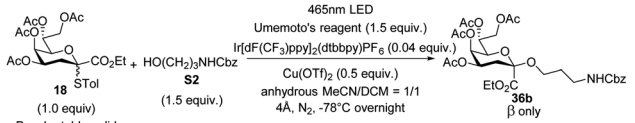

Entry	Amount of donor	Concentration	Yield[a]
1	32.4 mg	0.033 M	94%
2	324.3 mg	0.17 M	88%
3	1.04 g	0.19 M	$59\%^{40\%}$

[a] Isolated yields and the superscripts indicating the amount of donor regained.

Mechanism study

Activation of the donor. Based on the above experimental results, the mechanism of the photocatalytic Kdo *O*-glycosidation reaction could be divided into two parts: the activation of the donor to form the active intermediate and the reaction between the intermediate and acceptor to give the final product.

Considering that the activation of the donor is not affected by temperature (Table S2†), which only influences the subsequent attack on **34α** and **35β** (Scheme 1c) by the acceptor, to elucidate the underlying mechanism by which the photocatalyst $\mathbf{Ir^{III}}$ activates substrate **31**/**18**, we recorded the nanosecond transient absorption (ns-TA) spectra at room temperature for $\mathbf{Ir^{III}}$ alone and in a mixture with **31**/**18** under 430 nm laser excitation. As depicted in Scheme 4Ai–ii, upon laser excitation of $\mathbf{Ir^{III}}$ under N_2-saturated conditions, both the negative signals (negative bands at around 500 nm) and positive signals (a positive peak at around 440 and a featureless, flat absorption from 600 to 700 nm) are observed initially. The decay kinetics at 440, 500, and 700 nm all exhibit mono-exponential kinetics ($[OD] = [OD]_0\ e^{-k/t}$) with a consistent lifetime of 2.5 μs, suggesting the presence of a single transient species. This species is attributed to the triplet state ($^3\mathbf{Ir^{III*}}$) based on the strong spin–orbit coupling effect ($\xi_{Ir} = 3909\ M^{-1}\ cm^{-1}$), which facilitates rapid intersystem crossing from singlet to triplet states (<100 fs), and the sensitivity of the transient signal to oxygen (Fig. S3a†).[36–38] Therefore, the obtained lifetime of 2.5 μs corresponds to the photophysical decay process of $^3\mathbf{Ir^{III*}}$ to its ground state.

In the presence of **18**, the decay of $^3\mathbf{Ir^{III*}}$ is not affected (Scheme 4Aiii and S3b†). In contrast, for $\mathbf{Ir^{III}}$ in the presence of excess **31**, as shown in Scheme 4Aiv–vi, the decay of $^3\mathbf{Ir^{III*}}$ is significantly accelerated. This is consistent with the steady-state luminescence experiments: as more **31** is added, the luminescence intensity of $^3\mathbf{Ir^{III*}}$ decreases continuously (Fig. S3c†). Linear fitting of the measured pseudo-first-order reaction rate constants *versus* **31** concentration allows for the direct determination of the quenching efficiency of $^3\mathbf{Ir^{III*}}$ by using **31** ($4.0 \times 10^8\ M^{-1}\ s^{-1}$) (Scheme 4Avi). These findings suggest that the

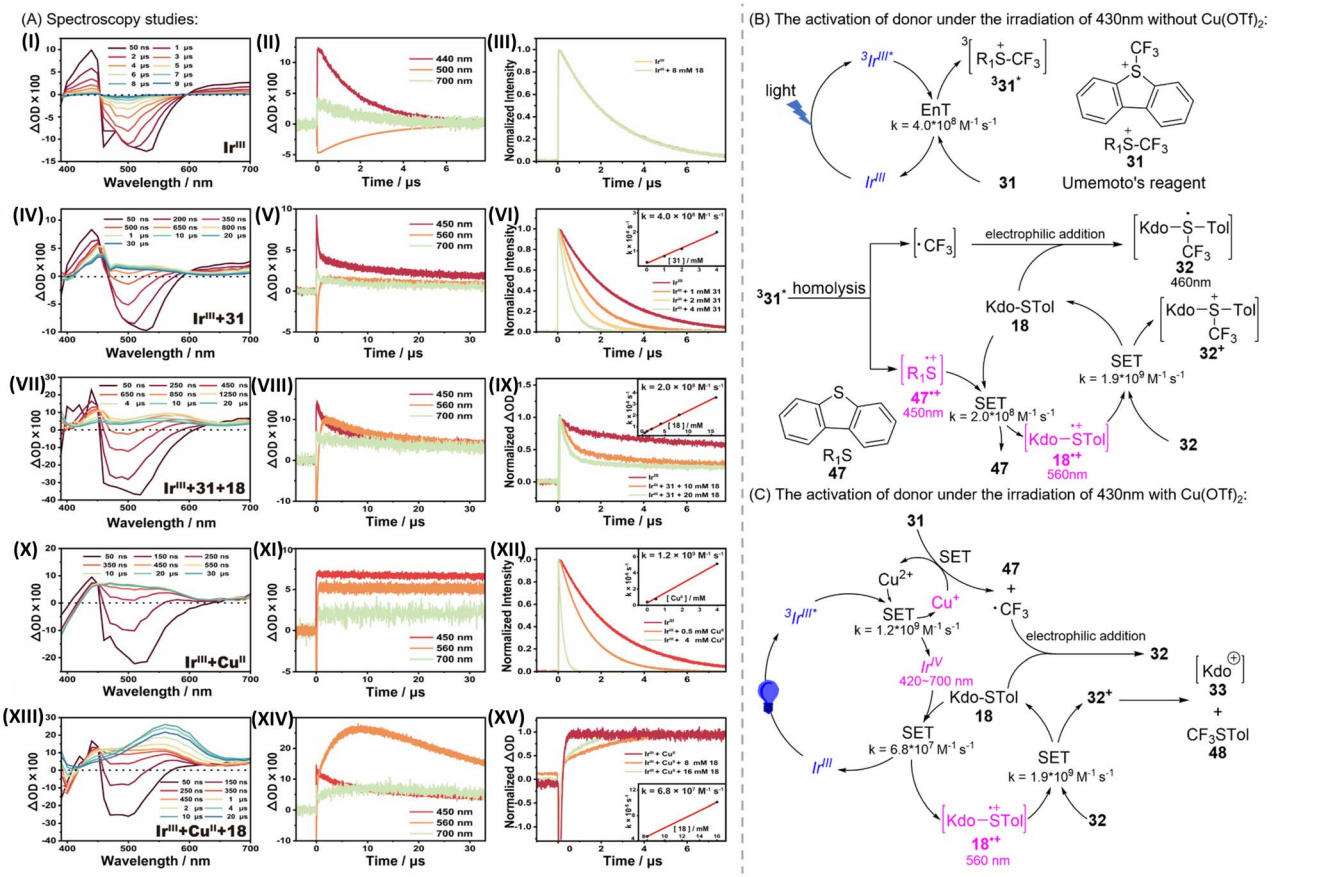

Scheme 4 (A) Spectroscopy studies: (I) transient absorption spectra of $^3\mathbf{Ir}^{\mathbf{III}*}$; (II) kinetics curves for transient absorption at 440, 500, and 700 nm of $^3\mathbf{Ir}^{\mathbf{III}*}$; (III) normalized transient emission kinetics of $^3\mathbf{Ir}^{\mathbf{III}*}$ at 500 nm in the absence and presence of **18**; (IV) transient absorption spectra of $^3\mathbf{Ir}^{\mathbf{III}*}$ + **31**; (V) kinetics curves for transient absorption at 450, 500, and 700 nm of $^3\mathbf{Ir}^{\mathbf{III}*}$ + **31**; (VI) normalized transient emission kinetics of $^3\mathbf{Ir}^{\mathbf{III}*}$ at 500 nm with different concentrations of **18**; inset: Stern–Volmer plot obtained from the decay of $^3\mathbf{Ir}^{\mathbf{III}*}$ with different concentrations of **18**; (VII) transient absorption spectra of $^3\mathbf{Ir}^{\mathbf{III}*}$ + **31** + **18**; (VIII) kinetics curves for transient absorption at 450, 560, and 700 nm of $^3\mathbf{Ir}^{\mathbf{III}*}$ + **31** + **18**; (IX) normalized kinetics curves for transient absorption at 450, 560, and 700 nm of $^3\mathbf{Ir}^{\mathbf{III}*}$ + **31** + **18**; inset: Stern–Volmer plot obtained from the decay of $^3\mathbf{Ir}^{\mathbf{III}*}$ + **31** at 450 nm with different concentrations of **18**. (X) Transient absorption spectra of $^3\mathbf{Ir}^{\mathbf{III}*}$ + $\mathbf{Cu}^{\mathbf{II}}$; (XI) kinetics curves for transient absorption at 450, 560, and 700 nm of $^3\mathbf{Ir}^{\mathbf{III}*}$ + $\mathbf{Cu}^{\mathbf{II}}$; (XII) normalized transient emission kinetics of $^3\mathbf{Ir}^{\mathbf{III}*}$ at 500 nm with different concentrations of $\mathbf{Cu}^{\mathbf{II}}$; inset: Stern–Volmer plot obtained from the decay of $^3\mathbf{Ir}^{\mathbf{III}*}$ with different concentrations of $\mathbf{Cu}^{\mathbf{II}}$; (XIII) transient absorption spectra of $^3\mathbf{Ir}^{\mathbf{III}*}$ + $\mathbf{Cu}^{\mathbf{II}}$ + **18**; (XIV) kinetics curves for transient absorption at 450, 560, and 700 nm of $^3\mathbf{Ir}^{\mathbf{III}*}$ + $\mathbf{Cu}^{\mathbf{II}}$ + **18**; (XV) normalized kinetics curves for transient absorption for $^3\mathbf{Ir}^{\mathbf{III}*}$ + $\mathbf{Cu}^{\mathbf{II}}$ at 560 nm with different concentrations of **18**; inset: Stern–Volmer plot obtained from the decay of $^3\mathbf{Ir}^{\mathbf{III}*}$ + $\mathbf{Cu}^{\mathbf{II}}$ with different concentrations of **18**. Experimental conditions (unless otherwise stated): under deoxygenated conditions in MeCN solution at 430 nm. The concentrations of $\mathbf{Ir}^{\mathbf{III}}$, $\mathbf{Cu}^{\mathbf{II}}$, **31**, and **18** used are 400 μM, 8 mM, 8 mM, and 8 mM, respectively. (B) Proposed mechanism of the activation of glycosidation under 430 nm irradiation without $Cu(OTf)_2$. (C) Proposed mechanism of the activation of glycosidation under 430 nm irradiation with $Cu(OTf)_2$.

entire photocatalytic cycle is initiated by the quenching of $^3\mathbf{Ir}^{\mathbf{III}*}$ by **31**.

The efficient reaction of $^3\mathbf{Ir}^{\mathbf{III}*}$ + **31** is accompanied by the emergence of a new spectral shape within 1.5 μs, characterized by an absorption peak at around 450 nm and a broad band at around 540 nm (Scheme 4Aiv). According to Wu *et al.*'s work,[39] this quenching reaction proceeds through a Dexter energy transfer catalytic mechanism: $^3\mathbf{Ir}^{\mathbf{III}*}$ transfers energy to **31**, resulting in $\mathbf{Ir}^{\mathbf{III}}$ and **31** in the triplet state (^{3}**31***). The generated triplet of **31** undergoes C–S σ-bond homo-cleavage, yielding $^{\bullet}CF_3$ and $R_1S^{\bullet+}$. In the illuminated $\mathbf{Ir}^{\mathbf{III}}$ + **31** system, the direct observation of both $^{\bullet}CF_3$ and $R_1S^{\bullet+}$ through ESR spectroscopy supports the above mechanism (Fig. S4†). Interestingly, such a new spectral shape is also observed when **31** is directly excited (Fig. S3d†). Upon direct light absorption, the substrate is expected to follow this pathway: excitation of **31** to the singlet excited state, followed by intersystem crossing (ISC) to ^{3}**31***, which induces homolytic cleavage. This control experiment provides additional evidence supporting the Dexter energy transfer mechanism mainly responsible for this quenching reaction.

The possible assignment of this new transient spectral shape as ^{3}**31*** or its subsequent homo-cleavage species ($^{\bullet}CF_3$ and/or $R_1S^{\bullet+}$), was further assessed. First, the decay of these new transient signals is independent of the oxygen concentration, which excludes the ascription as ^{3}**31*** (Fig. S3e†). Indeed, C–S σ-bond homo-cleavage of ^{3}**31*** should be very fast, resulting in the immediate conversion of ^{3}**31*** into homolytically cleaved radical

species ($^{\bullet}CF_3$ and $R_1S^{\bullet+}$), preventing the detectable accumulation of $^3\mathbf{31}^*$. Second, the $^{\bullet}CF_3$ radical is expected to absorb primarily in the UV region, as supported by our TD-DFT calculations (Fig. S5a†). In contrast, the calculated spectrum of $R_1S^{\bullet+}$ is in good agreement with this new spectral shape (Fig. S5b†). These results suggest that the observed spectrum should be assigned to the $R_1S^{\bullet+}$, rather than $^3\mathbf{31}^*$ or $^{\bullet}CF_3$. The observation of $R_1S^{\bullet+}$ supports that Dexter energy transfer is the dominant pathway, rather than the electron transfer from $^3\mathbf{Ir^{III}}^*$ to **31**. The latter would result in **47** (ref. 40) (Scheme 4B) and $^{\bullet}CF_3$ (Fig. S5a†), neither of which have a characteristic signal above 400 nm. Nevertheless, we cannot completely rule out the contribution of the electron transfer mechanism from $^3\mathbf{Ir^{III}}^*$ to **31**, based on the following points: (1) the oxidation potential of $^3\mathbf{Ir^{III}}^*$ (−0.65 V (ref. 41)) and the reduction potential of **31** (−0.06 V (ref. 42)). The potential difference indicates that electron transfer is thermodynamically feasible (Table S6†). (2) The new spectral shape obtained from the efficient reaction of $^3\mathbf{Ir^{III}}^*$ + **31** differs slightly from the spectrum after photolysis of **31** alone (Fig. S3f†). This difference may result from the contribution of $\mathbf{Ir^{IV}}$ produced by the electron transfer from $^3\mathbf{Ir^{III}}^*$ to **31**.

After elucidating that the photocatalytic cycle begins with Dexter energy transfer from $^3\mathbf{Ir^{III}}^*$ to **25**, leading to $^3\mathbf{31}^*$ and its conversion into radicals ($^{\bullet}CF_3$ and $R_1S^{\bullet+}$), and subsequently identifying $R_1S^{\bullet+}$ as the observed spectral species, we measured the transient absorption spectra and kinetics for $^3\mathbf{Ir^{III}}^*$ + **31** + **18**. As shown in Scheme 4Avii–ix, after introducing excess **18**, the decay of the transient absorption at around 450 nm for $R_1S^{\bullet+}$ was significantly accelerated, with a concomitant build-up of a new broad band at around 560 nm. Linear fitting of the measured pseudo-first-order reaction rate constants *versus* **18** concentration yields the second-order rate constant for the reaction $R_1S^{\bullet+}$ + **18** (2.0×10^8 M^{-1} s^{-1}) (Scheme 4Aix). These results demonstrate that **18** can efficiently quench $R_1S^{\bullet+}$. Our DFT calculations on the standard free energy change indicate that the electron transfer from **18** to $R_1S^{\bullet+}$ is thermodynamically favorable (Table S7†). Moreover, TD-DFT calculations show that the calculated spectrum of $\mathbf{18}^{\bullet+}$ matches well with the spectrum shape at around 560 nm, suggesting the assignment of this new spectral feature as $\mathbf{18}^{\bullet+}$ (Fig. S5c†). The appearance of $\mathbf{18}^{\bullet+}$ from the reaction $R_1S^{\bullet+}$ + **18** provides direct evidence for the electron transfer from **18** to $R_1S^{\bullet+}$.

This transient signal at around 560 nm for $\mathbf{18}^{\bullet+}$ decays on a much longer timescale. By analyzing the decay kinetics at 560 nm, we found that instead of first-order kinetics (mono exponential decay behavior), the decay of $\mathbf{18}^{\bullet+}$ can be approximated by using second-order reaction behavior (Fig. S3g†). This suggests that the decay of $\mathbf{18}^{\bullet+}$ likely results from reactions with species of comparable concentration in the system. These species include $^{\bullet}CF_3$ or its subsequent transformations. Considering that $^{\bullet}CF_3$ is electrophilic, it can effectively undergo electrophilic addition reactions with thioglycosides (**18**) containing lone pairs on sulfur atoms, leading to rapid quenching and the formation of **32**. Therefore, we propose that **32**, rather than the $^{\bullet}CF_3$ radical, is more likely responsible for quenching $\mathbf{18}^{\bullet+}$. The quenching process of $\mathbf{18}^{\bullet+}$ by **32** is expected to most likely be through the electron transfer pathway, leading to the re-generation of **18** and formation of $\mathbf{32}^+$. The structure of $\mathbf{32}^+$ is quite unstable and decomposes into species **33** and **48** *via* C–S band cleavage. This heterolytic dissociation process is supported by our DFT calculations, which predict a barrier-free reaction potential for the conversion of $\mathbf{32}^+$ into **33** and **48** (Fig. S6†). Species **33** can further transform into the target product. Experimental observations of species **48** (ref. 20) (Scheme 4C) and the target product also support the above reaction pathway. Based on the calculated extinction coefficients for **32** and $\mathbf{18}^{\bullet+}$ at 560 nm (31 and 7176 L M^{-1} cm^{-1}, respectively), we determined the second-order reaction rate constant for **32** + $\mathbf{18}^{\bullet+}$ through kinetic fitting of the decay at 560 nm (1.9×10^9 M^{-1} s^{-1}) (Fig. S3g, S5c and d†).

The results of the steady-state experiments indicate that the introduction of $\mathbf{Cu^{II}}$ enhances the efficiency and yield of the reaction. To elucidate its role, we further examined the impact of $\mathbf{Cu^{II}}$ on the underlying reaction mechanism and kinetics of the photocatalytic cycle. As shown in Scheme 4Ax–xii, it was found that $\mathbf{Cu^{II}}$ could efficiently quench $^3\mathbf{Ir^{III}}^*$, with the quenching being linearly dependent on the concentration of $\mathbf{Cu^{II}}$ (1.2×10^9 M^{-1} s^{-1}). After $^3\mathbf{Ir^{III}}^*$ is quenched by $\mathbf{Cu^{II}}$, a new transient spectrum is observed (Scheme 4Ax). This includes a negative signal at around 400 nm and positive signals from 420 to 700 nm, with a broad band at around 490 nm, together with a shoulder at around 560 nm. The decay of these new spectral signals is not affected by oxygen (Fig. S3h†). Therefore, rather than being triplet species generated from the potential Dexter energy transfer from $^3\mathbf{Ir^{III}}^*$ to $\mathbf{Cu^{II}}$, these new spectral signals are expected to result from electron transfer between $^3\mathbf{Ir^{III}}^*$ and $\mathbf{Cu^{II}}$. Given that the new spectral signals do not display the spectral features of $\mathbf{Ir^{II}}$,[43–45] characterized by two resolved absorption bands at around 490 and 525 nm, we propose that, rather than a reductive quenching, the reaction between $^3\mathbf{Ir^{III}}^*$ and $\mathbf{Cu^{II}}$ is likely an oxidative quenching, resulting in $\mathbf{Ir^{IV}}$ and $\mathbf{Cu^{I}}$. Besides, the calculated negative ΔG also suggests that electron transfer from $^3\mathbf{Ir^{III}}^*$ to $\mathbf{Cu^{II}}$ is thermodynamically favorable, based on the oxidation potential of $^3\mathbf{Ir^{III}}^*$ (−0.65 V (ref. 41)) and the reduction potential of $\mathbf{Cu^{II}}$ (+1.21 V (ref. 46)). The generated species, $\mathbf{Ir^{IV}}$ and $\mathbf{Cu^{I}}$, can further complete the catalytic cycle through electron acceptance and donation, respectively. Subsequently, we explored the possible quenching species for $\mathbf{Ir^{IV}}$ and $\mathbf{Cu^{I}}$, separately. In the $^3\mathbf{Ir^{III}}^*$ + $\mathbf{Cu^{II}}$ system, the addition of **18** also resulted in the efficient generation of $\mathbf{18}^{\bullet+}$, characterized by the emergence of a band at around 560 nm (Scheme 4Axii–xiv). The formation of $\mathbf{18}^{\bullet+}$ increased with the increasing concentration of **18**, with a rate constant of 6.8×10^7 M^{-1} s^{-1} (Scheme 4Axv). This observation demonstrates that the substrate **18** can be oxidized by the sole oxidizing species in solution, $\mathbf{Ir^{IV}}$, through a bimolecular electron transfer pathway, thus completing the $\mathbf{Ir^{IV}}/\mathbf{Ir^{III}}$ cycle. In contrast, previous reports suggested that the electron-donating species, $\mathbf{Cu^{I}}$, can transfer an electron to the substrate **31**, which upon receiving the electron, generates dibenzothiophene (**47**, Scheme 4B), $^{\bullet}CF_3$, and $\mathbf{Cu^{II}}$, thus achieving $\mathbf{Cu^{I}}/\mathbf{Cu^{II}}$ cycling.[47,48]

Interestingly, we observed that the transient signals of $\mathbf{18}^{\bullet+}$ generated in the $^3\mathbf{Ir^{III}}^*$ + $\mathbf{Cu^{II}}$ + **18** reaction are notably stronger

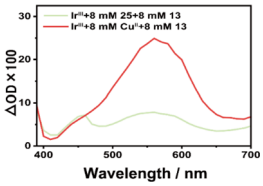

Fig. 3 Transient absorption spectrum obtained at 10 μs for ^{3}Ir^{III*} + **31** + **18**, in comparison with that for ^{3}Ir^{III*} + Cu^{II} + **18**. Experimental conditions (unless otherwise stated): under deoxygenated conditions in MeCN solution at 430 nm. The concentrations of Ir^{III}, **31**, **18**, and Cu^{II} used are 400 μM, 8 mM, 8 mM, and 8 mM, respectively. Note: the absorption peak at around 460 nm could be assigned to **32** supported by the calculated spectrum of **32** shown in Fig. S5d.†

than in the ^{3}Ir^{III*} + **31** + **18** system (Fig. 3). In both systems, ^{3}Ir^{III*} is effectively quenched by Cu^{II} or **31**. This indicates that the generation of **18**$^{\cdot+}$ through Ir^{IV}/Ir^{III} and Cu^{I}/Cu^{II} cycles is more effective compared to the Dexter energy transfer from ^{3}Ir^{III*} to **31** followed by oxidation of **18** by $R_1S^{\cdot+}$. The increased generation of **18**$^{\cdot+}$ is expected to result in more products, explaining why the addition of Cu^{II} enhances the efficiency of the entire photocatalytic reaction.

Besides, the much higher second-order rate constant for Cu^{II}-quenched ^{3}Ir^{III*} (1.2×10^9 M^{-1} s^{-1}), compared with **31**-quenched ^{3}Ir^{III*} (4.0×10^8 M^{-1} s^{-1}), demonstrates the superior photon utilization efficiency of the electron transfer quenching mechanism to that of its energy transfer counterpart. Incorporating Cu^{II} preserves the energy transfer pathway of ^{3}Ir^{III*} quenching while introducing an additional electron transfer pathway. This dual-pathway mechanism enhances overall ^{3}Ir^{III*} quenching efficiency, thereby markedly improving total photon utilization. This enhanced photon utilization, facilitated by the Cu^{II}-mediated electron transfer mechanism, also leads to increased generation of **18**$^{\cdot+}$ radicals, which would result in more products.

Stereoselectivity of glycosidation

Based on the experimental results shown in Tables 1, S3–S4† and Scheme 2 & 3 the selectivity of photocatalytic Kdo *O*-

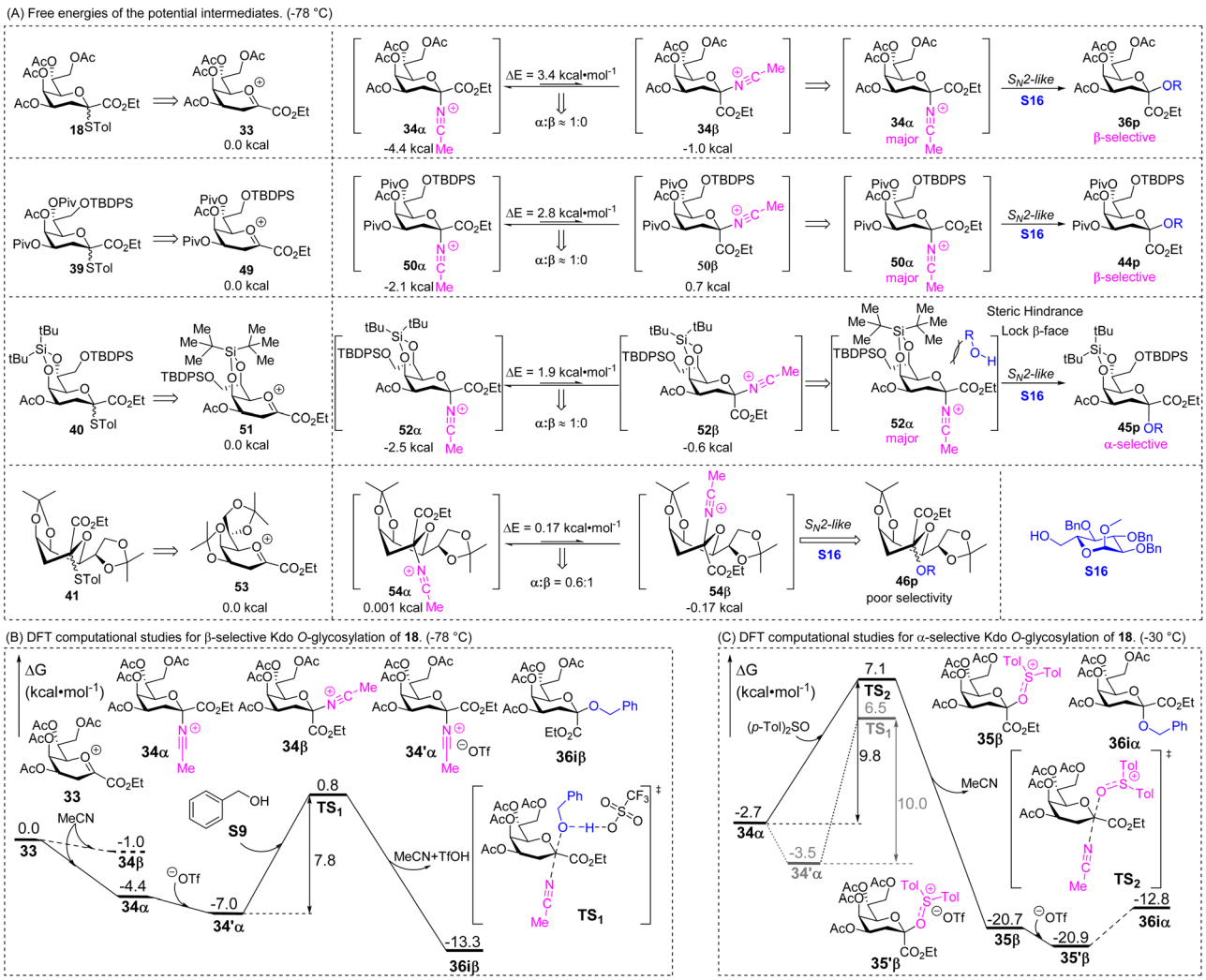

Scheme 5 DFT calculation studies determined at B3LYP-D3(BJ)/6-311+G(d, p) in the MeCN/DCM = 1 : 1 mixed solvent system (SMD).[32] (A) Free energies of potential intermediates at −78 °C. (B) Free energy profile of the formation of **36iβ** with benzyl alcohol **S9** as the acceptor at −78 °C. (C) Free energy profile of the formation of **36iα** with (*p*-Tol)$_2$SO as the additive at −30 °C.

glycosidation was highly controlled by acetonitrile and (p-Tol)$_2$SO. After forming the intermediate oxacarbenium ion **33**, it would be stabilized by MeCN to generate the less active intermediate glycosyl nitrilium ions **34** immediately at −78 °C (Scheme 5A). Based on the DFT method, benzyl alcohol **S9** was selected to further explore the mechanism from intermediates **33** (Scheme 5B). Due to the evident free energy difference (3.4 kcal mol^{-1}) between **34α** and **34β**, the reaction would proceed through **34α** (99.98%), according to the Boltzmann distribution. The intermediate is further combined with the trifluoromethanesulfonic anion to generate more stable species **34′α**. Then nucleophile **S9** subsequently approaches the anomeric carbon from the β-face *via* a S_N2-like transition state **TS1** to form MeCN, TfOH and product **36iβ**, accompanied by a hydrogen transfer from the hydroxyl group of benzyl alcohol to the TfO^- ion. The free energy barrier of this step is 7.8 kcal mol^{-1}.

For other Kdo glycosyl donors with a chair conformation ($^4C_1$) and electron-withdrawing groups, such as **39** (Scheme S1†), the free energy differences of the glycosyl nitrilium ions (**50α**/**50β**) are similar to that of **34α**/**34β**, which results in β-stereoselectivity (Scheme 5A). The bulky protecting group in donor **40** acts as a more significant factor, restricting the reaction space on the donor's β-face and resulting in α-stereoselectivity. When using **41** as the donor, the twist-boat conformation of **41** results in the different energy differences of **54α**/**54β**, thereby reducing the reaction selectivity (Scheme 5A).

When adding additive (p-Tol)$_2$SO in the glycosidation at −30 °C, the glycosyl nitrilium ion **34α** with a free energy of −2.7 kcal mol^{-1} is first attacked by (p-Tol)$_2$SO from the β-face to generate the more stable intermediate **35β** with a free energy of −20.7 kcal mol^{-1} through the transition state **TS2** (Scheme 5C). Then **35β** is stabilized by the TfO^- ion to generate **35′β** with a free energy of −20.9 kcal mol^{-1} and further reacts with the nucleophile **S9** *via* the S_N2-like transition state **TS3** to produce the product **36iα**, which is reported in our previous work.[14] Since the acceptor **S9** is a primary alcohol with strong nucleophilic properties and low steric hindrance, for the rate-limiting step **34α** → **TS2** (9.8 kcal mol^{-1}), compared with the free energy barrier of the direct attack of **34′α** by **S9** to obtain product **36iβ** (10.0 kcal mol^{-1}), the tiny difference between them makes the stereoselectivity poor ($\alpha/\beta = 0.9:1$). But for other acceptors with less nucleophilic properties and larger steric hindrance, the energy difference might be obvious and the direct attack of **34α** by acceptors might be harder, leading to higher α-selectivity.

On the basis of the mechanism study above, two plausible and substantiated catalytic cycles were drawn as shown in Scheme 4B and C. **Ir^{III}** is first excited to reach the triplet state **^{3}Ir^{III*}**. Through the single electron transfer (SET) process, **Cu^{II}** is reduced into **Cu^{I}** by **^{3}Ir^{III*}**, followed by the oxidation of **Cu^{I}** with Umemoto's reagent to generate **47** and $^{\cdot}CF_3$. The electrophile $^{\cdot}CF_3$ immediately binds with the excess thioglycoside donor **18** to produce intermediate **32** (Scheme 4C). Meanwhile, the donor **18** is oxidized into **18$^{\cdot+}$** by **Ir^{IV}**. Through the SET reaction between **32** and **18$^{\cdot+}$**, **32$^+$** is generated and immediately decomposes into species **48** and **33**. Notably, it is necessary to consider the EnT process at the activation stage to form **33** (Scheme 4B). The intermediate **33** is further stabilized by MeCN or (p-Tol)$_2$SO to form **34′α** or **35′β**. Finally, the nucleophile ROH attacks the intermediate **34′α** or **35′β** *via* a S_N2-like mechanism to produce β- or α-Kdo *O*-glycosides (Scheme 5B and C).

Conclusions

In summary, a photocatalytic stereoselective Kdo *O*-glycosidation was developed using 4,5,7,8-tetra-*O*-acetyl-protected Kdo p-toluenethioglycoside **18** as the donor. Based on such a strategy, the α- and β-Kdo *O*-glycosides could be switchably synthesized by adding (p-Tol)$_2$SO or not. With the special photoreactor improved by us, from the primary alcohol acceptors and several secondary alcohols, β-Kdo *O*-glycosides could be obtained efficiently for the complex saccharide synthesis. The detailed mechanism studies first showed that both EnT and SET processed could be preserved at the initiation stage and copper(II) was the key catalyst in the SET process. Further DFT calculation indicated that the photocatalytic Kdo *O*-glycosidation proceeds *via* the S_N2-like mechanism (Scheme 1d). This work pioneered a photocatalytic glycosidation method for Kdo *O*-glycosidation and provided a practical MeCN/(p-Tol)$_2$SO dual mediated strategy for α-/β-switchable stereoselective glycosidation. The detailed mechanism revealed by laser flash photolysis and steady-state spectral measurement offered a novel framework for understanding the activation processes in photocatalytic glycosidation reactions.

Data availability

The data supporting this article have been included as part of the ESI.†

Author contributions

Conceptualization, J.-d. Zhang and J.-l. Jie; methodology, J.-d. Zhang and J.-l. Jie; validation, J.-d. Zhang and S.-y. Yan; formal analysis, J.-d. Zhang, J.-l. Jie and S.-y. Yan; investigation, J.-d. Zhang, J.-l. Jie, S.-y. Yan, H. Zhang, J.-m. Chen, J.-c. Wu, L.-y. Qin and G.-j. Liu; visualization, J.-d. Zhang and S.-y. Yan; writing – original draft, J.-d. Zhang and J.-l. Jie; writing – review & editing, J.-d. Zhang, J.-l. Jie, H.-m. Su and G.-w. Xing; funding acquisition, J.-l. Jie, H.-m. Su and G.-w. Xing; resources, J.-l. Jie, H.-m. Su and G.-w. Xing; supervision, J.-l. Jie, H.-m. Su and G.-w. Xing.

Conflicts of interest

There are no conflicts to declare.

Acknowledgements

This work was supported by the National Natural Science Foundation of China (No. 21977014, 21907008, 21933005, and 22473014), and the National Key R&D Program of China (No. 2022YFA1505400).

Notes and references

1 F. M. Unger, *Adv. Carbohydr. Chem. Biochem.*, 1981, **38**, 323–388.
2 L. Cipolla, L. Gabrielli, D. Bini, L. Russo and N. Shaikh, *Nat. Prod. Rep.*, 2010, **27**, 1618–1629.
3 S. G. Wilkinson, *Prog. Lipid Res.*, 1996, **35**, 283–343.
4 M. A. Schmidt and K. Jann, *Eur. J. Biochem.*, 1983, **131**, 509–517.
5 A. Laroussarie, B. Barycza, H. Andriamboavonjy, M. Tamigney Kenfack, Y. Blériot and C. Gauthier, *J. Org. Chem.*, 2015, **80**, 10386–10396.
6 O. G. Ovchinnikova, E. Mallette, A. Koizumi, T. L. Lowary, M. S. Kimber and C. Whitfield, *Proc. Natl. Acad. Sci. U. S. A.*, 2016, **113**, E3120–E3129.
7 For reviews on Kdo glycoside synthesis, see: (*a*) J. Hansson and S. Oscarson, *Curr. Org. Chem.*, 2000, **4**, 535–546; (*b*) T. K. Pradhan and K. K. T. Mong, *Isr. J. Chem.*, 2015, **55**, 285–296; (*c*) P. Kosma, *Tetrahedron Lett.*, 2016, **57**, 2133–2142; (*d*) T. Kumar Pradhan, *Eur. J. Org Chem.*, 2023, **26**, e202300146.
8 S. Oscarson, *Carbohydr. Chem.*, 2012, **38**, 40–60.
9 For detailed introduction on Kdo *O*-glycosidation, see ESI:† (*a*) M. Imoto, N. Kusunose, Y. Matsuura, S. Kusumoto and T. Shiba, *Tetrahedron Lett.*, 1987, **28**, 6277–6280; (*b*) G. J. P. H. Boons, F. L. van Delft, P. A. M. van der Klein, G. A. van der Marel and J. H. van Boom, *Tetrahedron*, 1992, **48**, 885–904; (*c*) K. Mannerstedt, K. Ekelöf and S. Oscarson, *Carbohydr. Res.*, 2007, **342**, 631–637; (*d*) H. Yoshizaki, N. Fukuda, K. Sato, M. Oikawa, K. Fukase, Y. Suda and S. Kusumoto, *Angew. Chem., Int. Ed.*, 2001, **40**, 1475–1480; (*e*) J. Huang, W. Huang, X. Meng, X. Wang, P. Gao and J. Yang, *Angew. Chem., Int. Ed.*, 2015, **54**, 10894–10898; (*f*) S. Hamajima, N. Komura, H. Tanaka, A. Imamura, H. Ishida, H. Noguchi, T. Ichiyanagi and H. Ando, *Org. Lett.*, 2022, **24**, 8672–8676; (*g*) S. Hamajima, N. Komura, H. Tanaka, A. Imamura, H. Ishida, T. Ichiyanagi and H. Ando, *Molecules*, 2022, **28**, 102; (*h*) R. R. Schmidt and A. Esswein, *Angew. Chem., Int. Ed.*, 1988, **27**, 1178–1180; (*i*) A. Esswein, H. Rembold and R. R. Schmidt, *Carbohydr. Res.*, 1990, **200**, 287–305; (*j*) B. Pokorny and P. Kosma, *Chemistryopen*, 2015, **4**, 722–728; (*k*) K. Ikeda, S. Akamatsu and K. Achiwa, *Chem. Pharm. Bull.*, 1990, **38**, 279–281; (*l*) A. Sun, Z. Li, Y. Wang, S. Meng, X. Zhang, X. Meng, S. Li, Z. Li and Z. Li, *Angew. Chem., Int. Ed.*, 2024, **63**, e202313985; (*m*) A. Sun, Z. Li, S. Li, X. Meng, Z. Li and Z. Li, *Chin. Chem. Lett.*, 2025, **36**, 109972; (*n*) K. T. Mong, T. K. Pradhan, C. Chiu, W. Hung, C. Chen and Y. Wang, *Org. Chem. Front.*, 2020, **7**, 2179–2186; (*o*) K. Ekelöf and S. Oscarson, *Carbohydr. Res.*, 1995, **278**, 289–300; (*p*) T. K. Pradhan, C. C. Lin and K. T. Mong, *Org. Lett.*, 2014, **16**, 1474–1477; (*q*) M. Mazur, B. Barycza, H. Andriamboavonjy, S. Lavoie, M. Tamigney Kenfack, A. Laroussarie, Y. Blériot and C. Gauthier, *J. Org. Chem.*, 2016, **81**, 10585–10599; (*r*) W. Huang, Y. Zhou, X. Pan, X. Zhou, J. Lei, D. Liu, Y. Chu and J. Yang, *J. Am. Chem. Soc.*, 2018, **140**, 3574–3582; (*s*) S. Pramanik, S. Mondal, A. Chinarev, N. V. Bovin and J. Saha, *Chem. Commun.*, 2023, **59**, 10028–10031.
10 Q. Lou, Q. Hua, L. Zhang and Y. Yang, *Org. Lett.*, 2020, **22**, 981–985.
11 H. Miao, S. Lu, H. Chen, J. Shang, J. Zheng and Y. Yang, *Org. Biomol. Chem.*, 2024, **22**, 2365–2369.
12 X. Mi, Q. Lou, W. Fan, L. Zhuang and Y. Yang, *Carbohydr. Res.*, 2017, **448**, 161–165.
13 H. Miao, R. Yu, J. Zheng, J. Shang, L. Zhang, M. Ma and Y. Yang, *Org. Lett.*, 2024, **26**, 10634–10639.
14 J. Zhang, X. Gao, S. Liu, Z. Geng, L. Chang, Y. Liu, Q. Ma, G. Xing, G. Liu and D. Fang, *Org. Lett.*, 2023, **25**, 4150–4155.
15 N. Hoffmann, *Chem. Rev.*, 2008, **108**, 1052–1103.
16 J. M. R. Narayanam and C. R. J. Stephenson, *Chem. Soc. Rev.*, 2011, **40**, 102–113.
17 G. S. Kumar and Q. Lin, *Chem. Rev.*, 2021, **121**, 6991–7031.
18 For reviews on photocatalytic glycosidation, see: (*a*) H. Wang, P. Wu, X. Zhao, J. Zeng and Q. Wan, *Acta Chim. Sin.*, 2019, **77**, 231–241; (*b*) A. Chen, L. Xu, Z. Zhou, S. Zhao, T. Yang and F. Zhu, *J. Carbohydr. Chem.*, 2022, **40**, 361–400; (*c*) T. Ghosh and T. Nokami, *Carbohydr. Res.*, 2022, **522**, 108677; (*d*) D. J. Gorelik, S. P. Desai, S. Jdanova, J. A. Turner and M. S. Taylor, *Chem. Sci.*, 2024, **15**, 1204–1236.
19 J. Zhang, Z. Luo, X. Wu, C. Gao, P. Wang, J. Chai, M. Liu, X. Ye and D. Xiong, *Nat. Commun.*, 2023, **14**, 8025.
20 R. Mao, D. Xiong, F. Guo, Q. Li, J. Duan and X. Ye, *Org. Chem. Front.*, 2016, **3**, 737–743.
21 Y. Yu, D. Xiong, R. Mao and X. Ye, *J. Org. Chem.*, 2016, **81**, 7134–7138.
22 M. L. Spell, K. Deveaux, C. G. Bresnahan, B. L. Bernard, W. Sheffield, R. Kumar and J. R. Ragains, *Angew. Chem., Int. Ed.*, 2016, **55**, 6515–6519.
23 M. Krumb, T. Lucas and T. Opatz, *Eur. J. Org Chem.*, 2019, **2019**, 4517–4521.
24 E. A. Valenzuela, T. Duong, V. Pradeep, X. He, J. M. Dobson, S. Lee, K. Lopata and J. R. Ragains, *Angew. Chem., Int. Ed.*, 2025, e202508424.
25 Q. Dang, Y. Deng, T. Sun, Y. Zhang, J. Li, X. Zhang, Y. Wu and D. Niu, *Nature*, 2024, **632**, 313–319.
26 C. Zhang, H. Zuo, G. Y. Lee, Y. Zou, Q. Dang, K. N. Houk and D. Niu, *Nat. Chem.*, 2022, **14**, 686–694.
27 L. Li, X. Yin, Y. Jiang, Y. Xia, X. Wang, J. Li, H. Li, Y. Qin and J. Yang, *Org. Lett.*, 2024, **26**, 2103–2107.
28 P. Ngoje and D. Crich, *J. Am. Chem. Soc.*, 2020, **142**, 7760–7764.
29 J. Zhang, G. Liu and G. Xing, *Chem. Commun.*, 2025, **61**, 1677–1680.
30 H. Hori, T. Nakajima, Y. Nishida, H. Ohrui and H. Meguro, *Tetrahedron Lett.*, 1988, **29**, 6317–6320.
31 F. M. Unger, D. Stix and G. Schulz, *Carbohydr. Res.*, 1980, **80**, 191–195.
32 P. R. Andreana and D. Crich, *ACS Cent. Sci.*, 2021, **7**, 1454–1462.
33 T. Lu and Q. Chen, *Comput. Theor. Chem.*, 2021, **1200**, 113249.

34 D. Crich and W. Li, *Org. Lett.*, 2006, **8**, 959–962.
35 G. Liu, C. Li, X. Zhang, W. Du, Z. Gu and G. Xing, *Chin. Chem. Lett.*, 2018, **29**, 1–10.
36 L. Flamigni, A. Barbieri, C. Sabatini, B. Ventura and F. Barigelletti, *Photochemistry and photophysics of coordination compounds: iridium*, Springer, 2007.
37 G. J. Hedley, A. Ruseckas and I. D. W. Samuel, *J. Phys. Chem. A*, 2010, **114**, 8961–8968.
38 S. Tschierlei, A. Neubauer, N. Rockstroh, M. Karnahl, P. Schwarzbach, H. Junge, M. Beller and S. Lochbrunner, *Phys. Chem. Chem. Phys.*, 2016, **18**, 10682–10687.
39 T. Liu, T. Li, Z. Y. Tea, C. Wang, T. Shen, Z. Lei, X. Chen, W. Zhang and J. Wu, *Nat. Chem.*, 2024, **16**, 1705–1714.
40 T. H. Jepsen, M. Larsen, M. Jørgensen, K. A. Solanko, A. D. Bond, A. Kadziola and M. B. Nielsen, *Eur. J. Org Chem.*, 2011, **2011**, 53–57.
41 T. Koike and M. Akita, *Inorg. Chem. Front.*, 2014, **1**, 562–576.
42 Y. Yasu, T. Koike and M. Akita, *Angew. Chem., Int. Ed.*, 2012, **51**, 9567–9571.
43 Z. Lin, Q. Zhou, Y. Liu, C. Chen, J. Jie and H. Su, *Chem. Sci.*, 2024, **15**, 11919–11927.
44 Y. Qin, R. Sun, N. P. Gianoulis and D. G. Nocera, *J. Am. Chem. Soc.*, 2021, **143**, 2005–2015.
45 R. Sun, Y. Qin, S. Ruccolo, C. Schnedermann, C. Costentin and D. G. Nocera, *J. Am. Chem. Soc.*, 2019, **141**, 89–93.
46 M. Johnsson and I. Persson, *Inorg. Chim. Acta*, 1987, **127**, 15–24.
47 S. Barata-Vallejo, B. Lantaño and A. Postigo, *Chem.–Eur. J.*, 2014, **20**, 16806–16829.
48 C. Zhang, *Org. Biomol. Chem.*, 2014, **12**, 6580–6589.